



Structural characterization of the sporulation protein GerM from *Bacillus subtilis*

Jennyfer Trouve^a, Ahmed Mohamed^b, Francisco Leisico^c, Carlos Contreras-Martel^a, Bowen Liu^a, Caroline Mas^a, David Z. Rudner^d, Christopher D.A. Rodrigues^{b,*}, Cecile Morlot^{a,*}

^a Institut de Biologie Structurale (IBS), Univ. Grenoble Alpes, CEA, CNRS, 38044 Grenoble, France

^b The ithree institute, University of Technology, Sydney, Broadway NSW 2007, Australia

^c UCIBIO, Departamento de Química, Faculdade de Ciências e Tecnologia, Universidade Nova de Lisboa, Caparica, Portugal

^d Department of Microbiology and Immunobiology, Harvard Medical School, Boston MA 02115, USA

ARTICLE INFO

Keywords:

Specialized secretion systems
Sporulation
Endospores
GerM
GerMN domain
SigG

ABSTRACT

The Gram-positive bacterium *Bacillus subtilis* responds to starvation by entering a morphological differentiation process leading to the formation of a highly resistant spore. Early in the sporulation process, the cell asymmetrically divides into a large compartment (the mother cell) and a smaller one (the forespore), which will mature into a resistant spore. Proper development of the forespore requires the assembly of a multiprotein complex called the SpoIIIA-SpoIIQ complex or “A-Q complex”. This complex involves the forespore protein SpoIIQ and eight mother cell proteins (SpoIIIAA to SpoIIIAH), many of which share structural similarities with components of specialized secretion systems and flagella found in Gram-negative bacteria. The assembly of the A-Q complex across the two membranes that separate the mother cell and forespore was recently shown to require GerM. GerM is a lipoprotein composed of two GerMN domains, a family of domains with unknown function. Here, we report X-ray crystallographic structures of the first GerMN domain of GerM at 1.0 Å resolution, and of the soluble domain of GerM (the tandem of GerMN domains) at 2.1 Å resolution. These structures reveal that GerMN domains can adopt distinct conformations and that the core of these domains display structural similarities with ring-building motifs found in components of specialized secretion system and in SpoIIIA proteins. This work provides an additional piece towards the structural characterization of the A-Q complex.

1. Introduction

To transport molecules (small molecules, proteins or DNA) across their cell envelope, bacteria assemble large multi-protein complexes called specialized secretion systems (Chandran, 2013; Costa et al., 2015; Portaliou et al., 2016). Depending on their function and the nature of the bacterial cell envelope (Gram-negative or Gram-positive), these nanomachines span one or two lipid bilayers. Double-membrane-spanning secretion systems include the type 1 secretion system (T1SS), T2SS, T3SS, T4SS and T6SS found in Gram-negative bacteria (Costa et al., 2015), as well as a new putative member: the SpoIIIA-SpoIIQ complex (called the A-Q complex henceforth) required for endospore development (Morlot and Rodrigues, 2018). Although most sporulating bacteria are Gram-positive and are thus enveloped by a single lipid bilayer, the developing endospore (the forespore) gets surrounded by two lipid bilayers, one derived from the forespore and the other one

from the mother cell (Tan and Ramamurthi, 2014). The A-Q complex assembles in this double membrane around the forespore and is composed of proteins displaying similarities with core components of distinct secretion systems, suggesting that it might transport molecule(s) between the mother cell and forespore cytosols (Camp and Losick, 2008, 2009; Doan et al., 2009; Meisner et al., 2008). The most significant evidence for this model is the recent discovery that the A-Q complex contains an oligomeric ring (formed by SpoIIAG) that resembles those found in T3SS and that might participate in a trans-envelope conduit connecting the mother cell and forespore (Rodrigues et al., 2016a; Zeytuni et al., 2017). In addition, three other A-Q proteins (SpoIIAB, SpoIIAF and SpoIIAH) were shown to display structural similarities with components of T2SS and T3SS (Levdikov et al., 2012; Meisner et al., 2012; Zeytuni et al., 2018a,b). Despite this recent progress, the assembly mechanism and global architecture of the complex remain mysterious (Morlot and Rodrigues, 2018). Here, we provide

* Corresponding authors.

E-mail addresses: christopher.rodrigues@uts.edu.au (C.D.A. Rodrigues), cecile.morlot@ibs.fr (C. Morlot).

<https://doi.org/10.1016/j.jsb.2018.09.010>

Received 5 July 2018; Received in revised form 21 September 2018; Accepted 24 September 2018

Available online 25 September 2018

1047-8477/ © 2018 Elsevier Inc. All rights reserved.

structural insights into GerM, a protein recently shown to be involved in the assembly of the A-Q complex (Rodrigues et al., 2016b).

In response to nutrient depletion, sporulating bacteria enter a differentiation process called sporulation that leads to the development of dormant and stress-resistant cells called spores (Tan and Ramamurthi, 2014). The different steps in sporulation are governed by transcriptional programs based on the sequential activation of sporulation-specific sigma transcription factors (σ or σ) in the mother cell or in the forespore (Higgins and Dworkin, 2012; Hilbert and Piggot, 2004). After formation of an asymmetric septum, two cells of unequal size (a large one called the mother cell and a small one called the forespore) lie side by side. Remodeling of the septal cell wall then allows migration of the mother cell membrane around the forespore, a phagocytic-like process called engulfment. Ultimately, the forespore is released within the mother cell and is surrounded by two membranes (called the outer and inner forespore membranes) that define a periplasmic-like space called the intermembrane space. The A-Q complex assembles across the two forespore membranes during engulfment and is required for σ G activation in the forespore, maintenance of the forespore physiological potential and spore development (Camp and Losick, 2009; Doan et al., 2009; Rodrigues et al., 2016b). This complex is composed of the forespore protein SpoIIQ and 8 mother cell proteins encoded by the *spoIIIA* operon (SpoIIIAA to SpoIIIAH, called AA to AH henceforth) (Guillot and Moran, 2007; Londono-Vallejo et al., 1997). All the A-Q proteins are membrane proteins except AA, which is a soluble ATPase (Doan et al., 2009). Most of the SpoIIIA proteins share similarities to components of specialized secretion systems: AA resembles T4SS ATPases, AB shares a common fold with EpsF/GspF/PilC that tether the ATPase to the inner membrane complex in T2SS, the multi-transmembrane topology of AE is reminiscent of permease domains found in T1SS, and three other A-Q components (AF, AG and AH) possess ring-building motifs (RBMs) found in ring-forming proteins of T3SS, suggesting that the A-Q complex has been cobbled from different parts of well-defined secretion systems (Doan et al., 2009; Levdikov et al., 2012; Meisner et al., 2012; Rodrigues et al., 2016a; Zeytuni et al., 2017, 2018a,b). The hybrid nature of the A-Q complex might even extend beyond the family of secretion systems since AB also displays structural similarities with the component (the C-subunit) connecting cytosolic and membrane domains in bacterial V-ATPases, which are involved in aerobic ATP synthesis (Yokoyama et al., 1998; Zeytuni et al., 2018a).

Recently, a new protein named GerM has been implicated in the A-Q complex (Rodrigues et al., 2016b). This lipoprotein contains two GerMN (Germane) domains, a family of approximately 100 residue-long domains (Pfam10646) present in all major bacterial phyla, including *Firmicutes*, *Actinobacteria*, *Deinococcus-Thermus*, *Cyanobacteria*, *Spirochaetes* and *Proteobacteria* groups. Tandem copies (called GerMN1 and GerMN2 henceforth, Fig. 1A) of the GerMN domain are present in the sporulation and germination protein GerM found in the Firmicute phylum (Sammons et al., 1987; Slynn et al., 1994), while isolated GerMN domains are found in spore-formers and non-sporogenous Firmicutes, as well as in the other bacterial phyla listed above (Rigden and Galperin, 2008). The function of the GerMN domains is unknown so far. Similar to the *spoIIIA* and *spoIIQ* genes, deletion of the *gerM* gene results in collapsed forespores phenotype, deficient σ G activity and failure to produce heat-resistant spores (Doan et al., 2009; Rodrigues et al., 2016b). In addition, GerM was shown to be required for AG localization around the forespore and to partially compensate for the absence of AH in the localization of Q, indicating that GerM is involved in the assembly of the A-Q complex and might potentially be part of it (Morlot and Rodrigues, 2018; Rodrigues et al., 2016b). The structure of GerM and its exact role in the assembly of the A-Q complex remain undetermined.

Here, we report the *ab initio* crystal structure of the first GerMN domain of GerM at 1 Å resolution and the structure of the soluble full-length region of GerM at 2.1 Å resolution. These structures provide evidence that GerMN domains can adopt different conformations, and

reveal an interesting similarity between the core of the GerMN domains and RBMs found in ring-forming proteins from T3SS and from the A-Q complex. RBMs are structural arrangements composed of two α -helices folding against a three-stranded β -sheet; they establish homomeric interfaces required for the oligomerization of ring-forming proteins such as PrgK and PrgH from T3SS or AG from the A-Q complex (Bergeron et al., 2015; Rodrigues et al., 2016a; Schraidt and Marlovits, 2011; Worrall et al., 2016; Zeytuni et al., 2017). Interestingly, GerM was found to form an oligomer in the crystals but we could not provide evidence that GerM oligomerizes *in vivo* using structure-guided GerM mutants. We discuss these observations and propose hypotheses for the functions of GerM and GerMN domains.

2. Results and discussion

2.1. *Ab initio* crystallographic structure of the first GerMN domain of GerM

The purified construct encompassing the first GerMN domain of GerM (GerMN1, residues Thr76 to Glu213) formed large needle-shaped crystals which remarkably diffracted to a resolution of 1.0 Å (Fig. S1A and Table 1). We first tried to solve this structure by molecular replacement using the coordinates of a single GerMN domain available in the Protein Data Bank (PDB entry 5J7R). This GerMN domain is the sole folded region (residues 44–182) of a 184 residue-long uncharacterized lipoprotein (Uniprot ID A0A0H2YS46, called GerMN_{Cp} henceforth) from *Clostridium perfringens*. As expected given the low sequence identity (20% identity over 165 residues) between GerMN_{Cp} and GerMN1, molecular replacement was unsuccessful. We thus took advantage of the particularly high diffraction power of the GerMN1 crystals to determine *ab initio* phases using the ARCIMBOLDO_LITE program (<http://chango.ibmb.csic.es/>) (Sammito et al., 2013), which combines the location of model fragments like small α -helices with Phaser (McCoy et al., 2007) and density modification with SHELXE (Thorn and Sheldrick, 2013) (see the *Methods* section). This strategy yielded an electron density map from the correct positioning of two helices and the high quality of this map allowed building of the model of the GerMN1 domain from Thr76 until Asp208, present as a single copy in the asymmetric unit. The core of GerMN1 contains two helices (α 1 and α 2) sandwiched between a three-stranded β -sheet (β 3 β 4 β 5) and a twisted two-stranded antiparallel β -sheet (β 1 β 2) (Fig. 1B).

A search for structural homologues using the DALI server (Holm and Rosenström, 2010) confirmed the close similarity of GerMN1 with GerMN_{Cp} from *C. perfringens* (PDB entry 5J7R, *rmsd* (root mean square deviation) of 2.2 Å over 143 residues, Z-score = 12.0). The major difference between the two structures is the “open” versus “closed” conformation of the β 1 β 2 sheet in GerMN_{Cp} and GerMN1, respectively. In GerMN_{Cp}, the β 1 β 2 sheet positions away from the globular core of the protein, while in GerMN1 the β 1 β 2 sheet is packed against helices α 1 and α 2 (Fig. 1C). However, analysis of the asymmetric unit content in the GerMN_{Cp} crystal shows that the β 1 β 2 sheet of one molecule packs against the globular core of the neighboring molecule, mimicking the intramolecular packing of β 1 β 2 in GerMN1 (Fig. S1B) and involving many interface residues equivalent in position and nature (Fig. S2A). Altogether, these observations suggest that the two conformations might exist in GerMN domains. In an attempt to detect the “open” conformation in GerMN1, we characterized its soluble form using SAXS (Small Angle X-ray Scattering).

The GerMN1 experimental scattering profile (Fig. 1D) presents linear ranges in the Guinier plot with *R*_g of 1.46 nm, pointing to a homogenous sample in solution composed of GerMN1 monomers with a *M*_{w(0)} of 13.3 kDa. In order to compare the GerMN1 structure in solution and in the crystal, the low-resolution SAXS envelope of GerMN1 in solution was generated using DAMMIF, and the scattering curve from GerMN1 crystal structure was computed using the CRYSOLOG software. Both experimental and computed scattering curves fit with a χ^2 of 2.1 (Fig. S1C), suggesting a similar GerMN1 structure in crystal and in

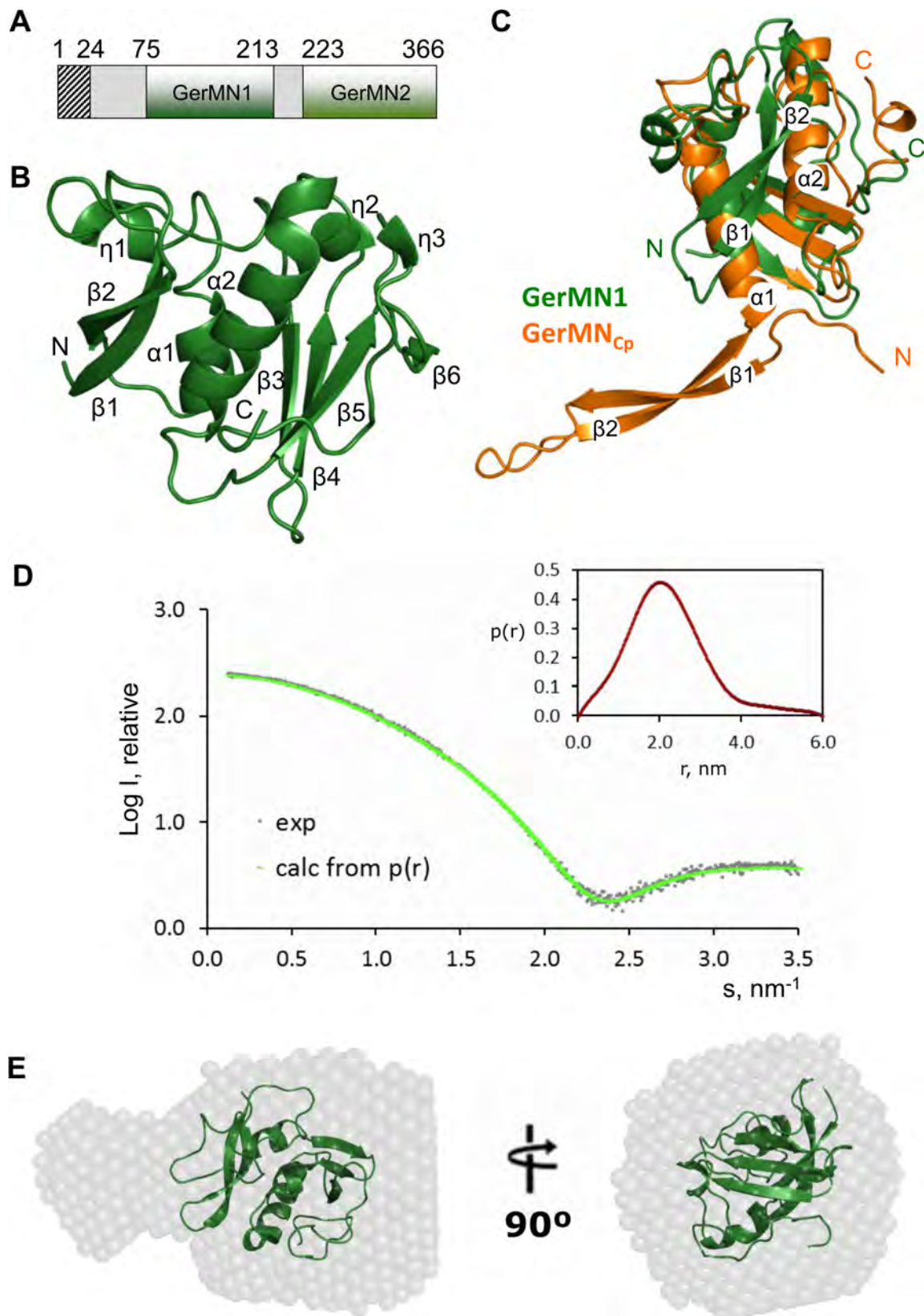


Fig. 1. *Ab initio* crystal structure of the first GerMN domain of GerM from *B. subtilis*. **A.** Domain structure of GerM showing the lipobox (hatched area), the first and second GerMN domains (GerMN1 in dark green and GerMN2 in light green). **B.** Ribbon representation of the GerMN1 domain of GerM. β -strands, α -helices, 3_{10} -helices (η), N- and C-termini are labeled. **C.** Overlay of the GerMN1 domain (in green) from *B. subtilis* GerM with GerMN_{cp} from *Clostridium perfringens* (in orange, PDB entry 5J7R) showing the “open” (in GerMN_{cp}) and “closed” (in GerMN1) conformations of the $\beta 1\beta 2$ sheet. Strands $\beta 1$ and $\beta 2$, helices $\alpha 1$ and $\alpha 2$, N- and C-termini are labeled. **D.** GerMN1 scattering data and distance distribution function. Fitting of the scattering curve computed from the $p(r)$ function (colored green) to the experimental scattering data of GerMN1 (colored grey). The insert shows the distance distribution function $p(r)$. **E.** GerMN1 crystal structure (green cartoon) fitted into the envelope of GerMN1 in solution, generated with DAMMIF (grey spheres) from the experimental scattering curve.

Table 1
Data collection and refinement statistics.

Data collection		
Name of dataset	4GerMN1_C2_1	5GerM1_B2_4
X-ray source	ID23eh1 (ESRF)	ID29 (ESRF)
Wavelength (Å)	0.97242	1.07252
Scan range (°)	102	160
Oscillation (°)	0.15	0.05
Space group	P2 ₁ 2 ₁ 2 ₁	P2 ₁ 2 ₁ 2 ₁
Unit-cell parameters		
a, Å	38.36	90.36
b, Å	53.60	103.94
c, Å	64.86	162.49
α, °	90.00	90.00
β, °	90.00	90.00
γ, °	90.00	90.00
Number of molecules in ASU	1	4
Resolution (last shell), Å	1.0 (1.06–1.0)	2.1 (2.22–2.1)
Completeness, %	94.5 (90.4)	99.8 (99.4)
I/σ(I)	11.22 (2.95)	17.83 (3.14)
Rsym [†] , %	6.1 (35.6)	5.9 (53.8)
Unique reflections	68,958 (10428)	89,726 (13589)
Observed reflections [I/σ(I) > 1]	250,905 (34925)	536,084 (79503)
Wilson B factor, (Å ²)	10.5	45.5
Refinement and model statistics		
Resolution (last shell), Å	1.00 (1.00–1.026)	2.1 (2.155–2.1)
R-factor [‡] , R-free [§]	0.135, 0.154	0.204, 0.236
rmsd from target [‡]		
Bond lengths, Å	0.008	0.004
Bond angle, °	1.33	0.740
Mean B factor (Å ²)	14.3	50.1
Ramachandran plot ^{**}		
Core, %	98.4	97.0
Allowed, %	1.6	2.9
Disallowed, %	0	0.1

Values in parentheses are for the outermost shell of data.

[†] Rsym = $(\sum(\text{ABS}(I(h,i) - (I(h)))))/(\sum(I(h,i)))$.

[‡] R-factor = $\sum|jF_{\text{obs}} - jF_{\text{calc}}|/\sum jF_{\text{obs}}$ where F_{obs} and F_{calc} are the observed and calculated structure factor amplitudes, respectively.

[§] R-free is the R-factor calculated with 5% of the reflections chosen at random and omitted from refinement.

[‡] rmsd of bond lengths and bond angles from ideal geometry.

** Performed by Procheck.

solution. However, fitting of GerMN1 crystal structure into the SAXS envelope showed unoccupied volume extending from the main globular region (Fig. 1E). In addition, the linker between strand β2 and helix α1 positioned near this unoccupied volume, and fitting of GerMN_{Cp} in the SAXS envelope showed that the unoccupied extended region could accommodate a β1β2 sheet displaying an “open” conformation (Fig. S1D). These observations thus suggest that when GerMN1 is in solution, the β1β2 sheet might display some flexibility and occupy the elongated region of the low-resolution envelope. In agreement with this hypothesis, the distance distribution function (Fig. 1E, insert) yields a maximum particle dimension (D_{max}) of 6 nm, which is close to the length of the long axis of GerMN_{Cp}.

Interestingly, the DALI program also detected structural similarities between the α1β3β4α2β5 core of the GerMN1 domain and RBMs found in PrgK/PrgH components of the inner membrane platform in T3SS and in AF, AG and AH components of the A-Q complex (Fig. 2A–C) (Bergeron et al., 2015; Levnikov et al., 2012; Meisner et al., 2012; Rodrigues et al., 2016a; Zeytuni et al., 2017, 2018b). Although the sequence identity between GerMN domains and RBMs is very weak (lower than 15%), the αββαβ organization of secondary structures is conserved (Fig. 2D). GerMN1 superimposes onto the second RBM of PrgH from *Salmonella typhimurium* (PDB code 4G11, residues Glu225–Asp295), and RBMs of AG (PDB code 5WC3) and AH (PDB code 3UZ0) from *B. subtilis* with rmsds of 2.57, 3.06 and 3.02 Å, respectively (over 65, 65 and 64 residues, respectively) (Fig. 2A–C). These similarities suggest that similar to RBMs, GerMN domains might have an oligomerization function. GerMN1, however, was only found to form

monomers in solution using SAXS ($MM_{(0)}$ of 13.3 kDa). To investigate whether oligomers would form in the presence of the second GerMN domain, we then sought to characterize the full-length soluble region of GerM.

2.2. Structural characterization of GerM

A recombinant construct lacking the lipobox and encompassing the two GerMN domains (GerM_{26–366}, residues Phe26 to Phe366) was purified and crystallized as rectangle-shaped crystals that diffracted to a resolution of 2.1 Å (Table 1). GerM_{26–366} structure was solved by molecular replacement using the atomic coordinates of GerMN1 as a template for the two GerMN domains. The main chains of the four molecules in the asymmetric unit could be easily traced from Ser74 to Phe366 but no electron density was visible for residues Phe26 to Ala73. Mass spectrometry analyses performed on the purified protein and on dissolved crystals provided experimental molecular weights of 37,173.4 Da and 37,173.1 Da, respectively (Table S1). These values are very close to the expected molecular weight value (37,172.5 Da), indicating that the protein had not suffered from proteolytic degradation, and that absence of electron density corresponding to residues Phe26 to Ala73 is due to flexibility of this N-terminal region.

The two GerMN domains fold against each other in a compact arrangement displaying a butterfly shape (Fig. 3A). Each GerMN domain forms a wing and the two domains are connected by the C-terminal loop of GerMN1 and a short linker. The GerMN1 and GerMN2 domains, which display 20% sequence identity, superimpose with rmsd of 2.54 Å over 127 residues (Fig. 3B). The interface between the two GerMN domains buries a surface of 1093 Å² and involves many hydrophobic interactions, which include Y89, V91, L95, P96, I120, F125 and I210 from GerMN1, and Y239, V241, P242, L272 and F366 from GerMN2 (Fig. 3C and S2). The interface also involves a salt bridge established by the side chains of E213 and K245, and multiple hydrogens bonds including the side chains of D85, Y89, T94 and N123 from GerMN1, and of N234, E235, Y239, T244 and N362 from GerMN2 (Fig. 3D and S2).

As expected given the similar fold of the two GerMN domains, the α3β9β10α4β11 core of GerMN2 also resembles RBMs of PrgH, AG and AH onto which it superimposes with rmsds of 2.47, 3.24 and 2.61 Å, respectively (over 64, 66 and 63 residues, respectively) (Fig. S3). Despite the fact that no oligomer could be detected in solution by SEC-MALLS analysis (molecular weight of ~35 kDa, corresponding to a GerM_{26–366} monomer, Fig. S4), GerM_{26–366} forms a tetramer in the asymmetric unit of the crystal. If we call the four molecules by their respective chain identifiers, the dimers formed by chains A and B, B and C, and C and D superimpose with rmsds ranging from 0.42 to 0.66 Å² over 284 residues (Fig. 4A). As the dimer formed by chains D and A' (the crystallographic symmetry of chain A) is also similar to the dimers observed in the asymmetric unit, the crystallographic symmetries extend the GerM_{26–366} tetramer into a protein protofilament in which each molecule interacts with the adjacent one through a conserved dimerization interface (Fig. 4B). This interface involves hydrophobic interactions between P199 and P225 from one molecule, and L273 and V269 from the adjacent molecule (Fig. 4C). In addition, seven salt bridges are established by the side chains of K163, K268, D275 and E278 from one chain, and the side chains of K182, K191, D203, D208 and D219, from the neighboring chain. Finally, a dozen of hydrogen bonds are established and include residues N87, G88, K163, T214, G216, K268, V269 and E278 from one chain and residues D202, D203, L220, T221, R246, N249 and K252 from the adjacent molecule (Fig. 4C).

The fact that GerM_{26–366} oligomers are not detected in solution suggests that GerM's self-association may be weak, requiring the stability and high protein concentration of a crystalline environment to be visualized. GerM oligomers might, however, form *in vivo* when the protein reaches high local concentrations in the intermembrane space and/or when GerM interacts with A-Q components. To investigate this idea, we introduced mutations in residues located at the GerM_{26–366}

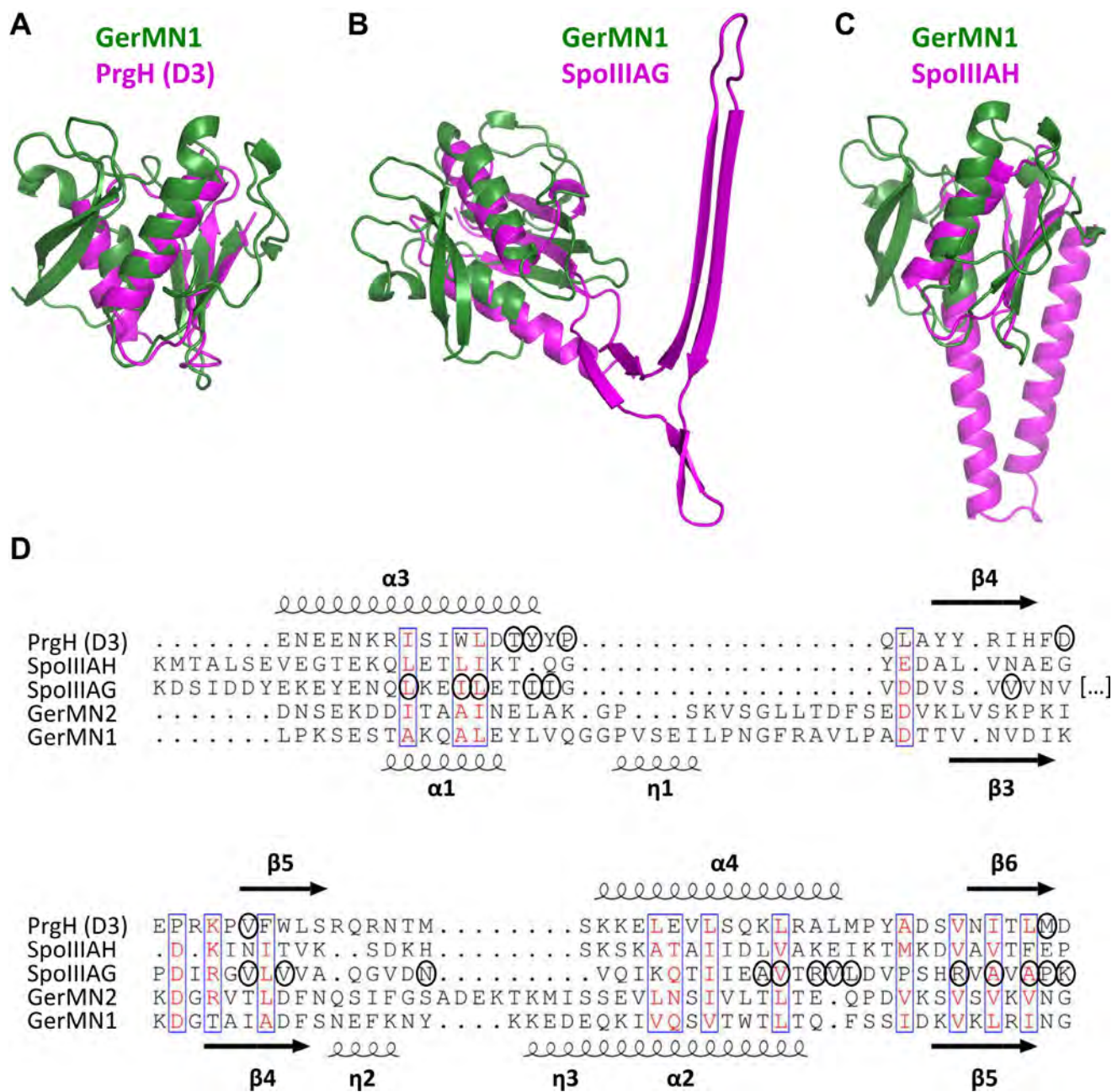


Fig. 2. Comparison of GerMN1 with RBM domains. A–C. Ribbon representations of GerMN1 (in dark green) superimposed onto the second periplasmic RBM of PrgH from *S. typhimurium* (A, PDB code 4G1I, in magenta), onto SpoIIIAG (B, PDB code 5WC3, in magenta) and onto SpoIIIAH (C, PDB code 3UZ0, in magenta) from *B. subtilis*. D. Sequence alignment of RBMs found in PrgH from *S. typhimurium* (second periplasmic domain, residues Glu225–Asp295, PrgH (D3)), SpoIIIAH and SpoIIIAG from *B. subtilis*, with the first (GerMN1) and second (GerMN2) GerMN domains of GerM from *B. subtilis*. The insertion region (Asp124 to Lys181) in the RBM of SpoIIIAG was omitted from the sequence alignment and represented with dots into brackets ([...]). Similar residues are shown by red letters boxed in blue. The secondary structures of PrgH (D3) and GerMN1 are indicated above and below the sequence alignment, respectively. Arrows indicate β -strands; α , α -helices; η , 3_{10} -helices. Residues at the RBM oligomerization interfaces are indicated by black circles.

dimerization interface observed in the crystal (Fig. S2B). When introduced in the recombinant GerM_{26–366} construct, four of these mutations (K268E, D219R, R246E and K252E) resulted in partial proteolysis of the protein (Table S1). Three mutations (D275R, D203R–D202R and E278R) did not affect the stability of GerM_{26–366} and were thus introduced *in vivo* in the context of the full-length *gerM* gene. All these mutations were able to rescue a null mutation of *gerM*, in the presence or in the absence of *spoIIIAH* (Table 2). Although it remains possible that a potential GerM oligomer might still be able to form despite these mutations, these data strongly suggest that the GerM homodimerization interface observed in the crystal is not physiological.

3. Conclusions

The structural characterization of GerM reported here reveals that the N-terminal β -sheet ($\beta 1\beta 2$) of GerMN domains can display different conformations. While the $\beta 1\beta 2$ sheet of the GerMN1 and GerMN2 domains of GerM display a “closed” conformation (packed against the core of the domain) in the crystals, SAXS analysis of GerMN1 is consistent with the hypothesis that the $\beta 1\beta 2$ sheet might display an “open” conformation in solution. The “closed” and “open” conformations of the $\beta 1\beta 2$ sheet might represent different functional states of the GerMN domains and might constitute a way to regulate their function in

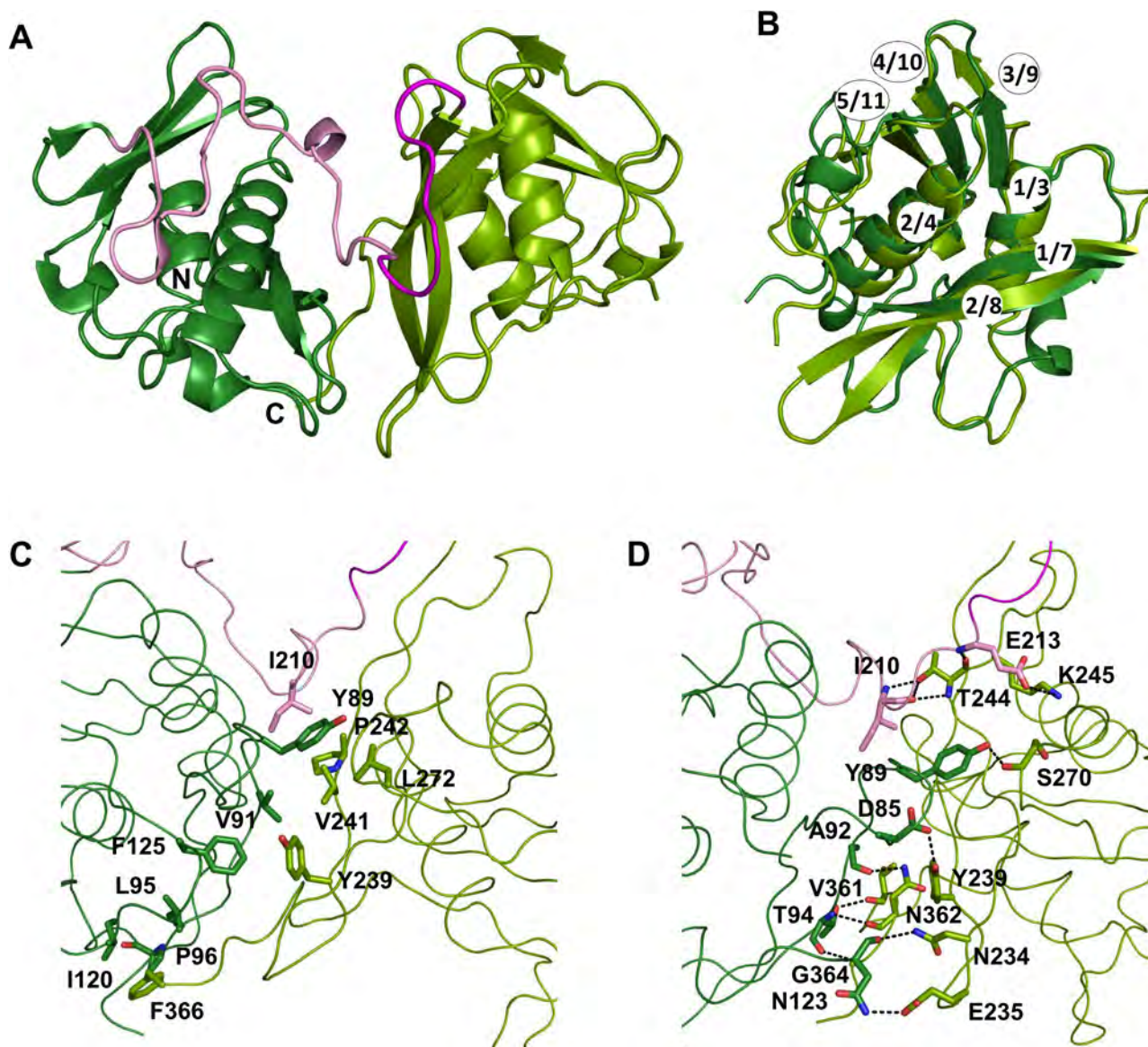


Fig. 3. Structure of GerM₂₆₋₃₆₆ from *B. subtilis*. **A.** Ribbon representation of GerM₂₆₋₃₆₆, with the GerMN1 and GerMN2 domains colored in dark and light green, respectively. The part of the GerMN1 domain belonging to the loop connecting GerMN1 and GerMN2 is colored in pink and the linker region in magenta. N- and C-termini are labeled. **B.** Superimposition of GerMN1 (in dark green) onto GerMN2 (in light green). N- and C-termini are labeled. Numbering of β -strands and α -helices are indicated for GerMN1/GerMN2. **C–D.** Views of the GerMN1–GerMN2 interface with residues involved in hydrophobic (**C**) or electrostatic (**D**) interactions labeled and shown as atom-colored sticks. The main chain of the protein is shown as a loop.

different environments (presence of protein partners, cellular location). This hypothesis will be investigated in the future.

In addition, our GerM structures reveal that the $\alpha\beta\beta\alpha\beta$ core of GerMN domains resembles RBMs found in ring-forming proteins such as PrgH from T3SS and AG, which is a central building block of the A-Q complex. In the GerM₂₆₋₃₆₆ crystal, we observe an oligomerization interface which is very different from the oligomerization interfaces observed for PrgH or AG RBMs, and we could not provide evidence that this crystalline interface is physiological. However, it remains possible that GerM oligomerizes *in vivo* through an interface that would resemble those of RBMs and require environmental conditions (interaction with the membrane and/or protein partners) that are missing in our *in vitro* experiments. AH was also proposed to oligomerize through its RBM domain. Redundancy of putative AH and GerM rings in the formation of a conduit at the core of the A-Q complex might thus explain why AH and GerM partially compensate each other in forespore development. This remains a highly speculative hypothesis because no oligomerization of AH or GerM has been demonstrated so far. In

addition, oligomerization of RBMs is difficult to predict because interface residues are very poorly conserved between different ring-forming proteins (Fig. 2D). Alternatively, although the core of GerMN domains display similarities with RBMs, the presence of additional N- and C-terminal elements (the $\beta 1\beta 2$ sheet and the C-terminal loop) might prevent RBM-like oligomerization and provide a totally different function for this family of domains. Consistent with this idea, the RBM domain of AH also contains an additional N-terminal element (the α -helix formed by residues Leu105 to Ser129) when compared to canonical RBMs, and no oligomerization was reported so far for AH. In addition, AH and GerM partially compensate each other for the localization of Q. Based on these observations, one might speculate that a function of non-canonical RBMs such as those present in AH and GerM might be to localize proteins.

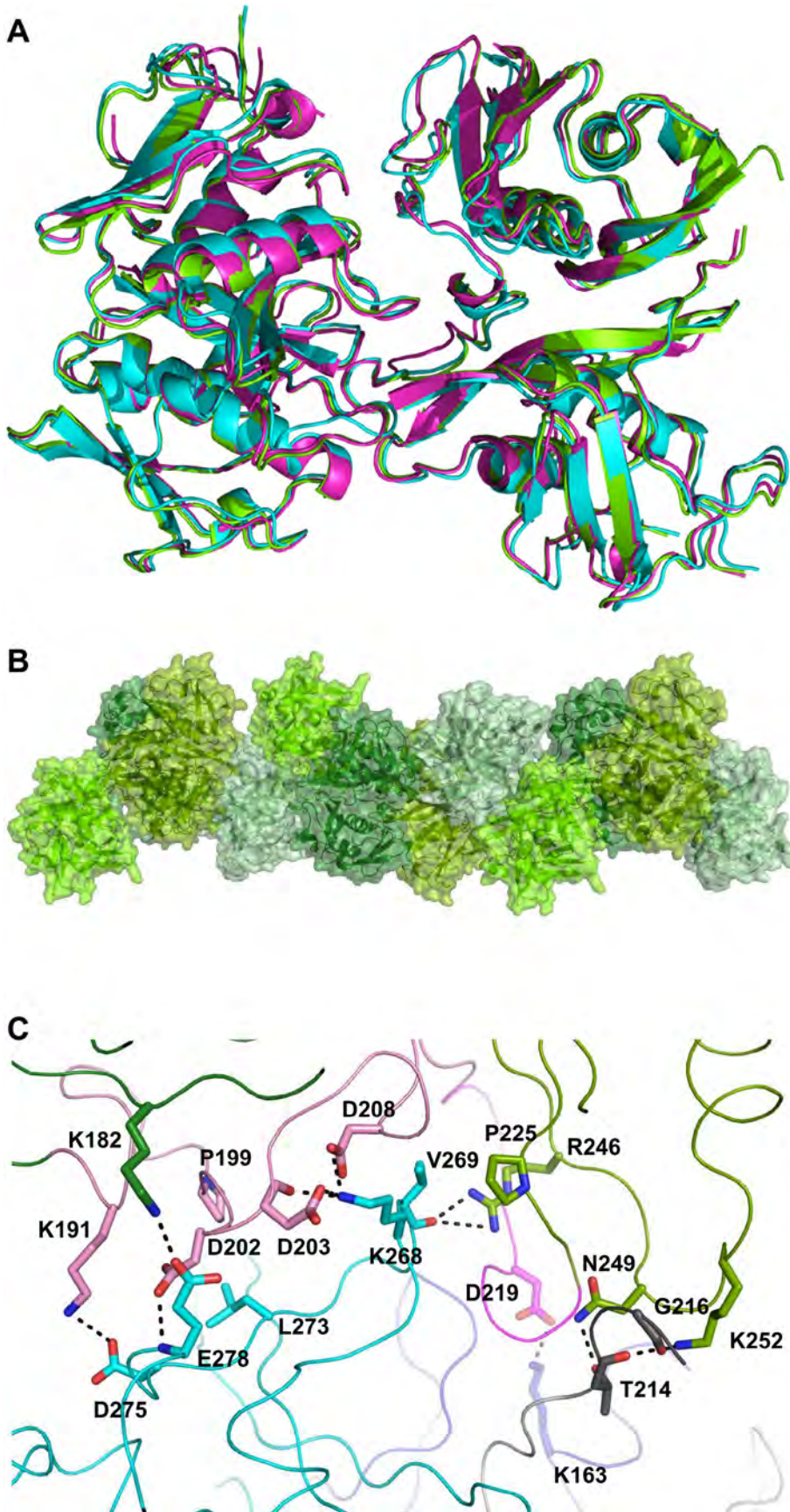


Fig. 4. GerM oligomerization in the crystal. **A.** Overlay of the GerM₂₆₋₃₆₆ dimers formed by chains A/B (in green), B/C (in cyan) and C/D (in magenta) in the asymmetric unit. **B.** GerM₂₆₋₃₆₆ protofilament resulting from the continued dimerization of GerM₂₆₋₃₆₆ molecules in the crystal. The protofilament is visualized upon display of the crystallographic symmetries of the asymmetric unit content. The four GerM₂₆₋₃₆₆ molecules in each asymmetric unit are colored in different shades of green and shown with ribbon and surface representations. **C.** View of the dimerization interface between two GerM₂₆₋₃₆₆ molecules in the crystal structure. Residues involved in hydrophobic or electrostatic interactions are labeled and shown as atom-colored sticks. The main chain of the protein is shown as a loop.

Table 2
Sporulation efficiency of *B. subtilis* strains expressing GerM interface mutants.

Strain	Genotype	Sporulation efficiency (%)
PY79	WT	100
BCR1237	Δ gerM	2.1
BCR287	Δ spoIIIAH	2.5
BAT0044	Δ gerM Δ spoIIIAH	0.002
BAT0075	Δ gerM gerM (D202R-D203R)	85.6
BAT0076	Δ gerM Δ spoIIIAH gerM (D202R-D203R)	0.9
BAT0047	Δ gerM gerM (D275R)	89.4
BAT0048	Δ gerM Δ spoIIIAH gerM (D275R)	1.1
BAT0094	Δ gerM gerM (E278R)	73.3
BAT0095	Δ gerM Δ spoIIIAH gerM (E278R)	2.2

4. Materials and Methods

4.1. Bacterial strains and plasmids

Strains, plasmids and oligonucleotides used in this study are listed in Table S2. All *B. subtilis* strains were derived from the prototrophic strain PY79 (Youngman et al., 1983).

4.2. Protein production and purification

All recombinant constructs were fused to a hexahistidine tag followed by the SUMO cleavage site of the Ulp1 protease (His-SUMO tag) (Marblestone et al., 2006) and overexpressed in *E. coli* BL21 (DE3) RIL cells. Cells were grown at 37 °C in 2 l of Terrific Broth (BD Biosciences) supplemented with ampicillin (100 µg/ml) until the OD_{600nm} reached 0.8. Production of recombinant proteins was induced by the addition of isopropyl β-D-1-thiogalactopyranoside (IPTG) to 0.5 mM after the cultures were cooled to 25 °C. Cell growth was continued overnight at 25 °C, and cells were harvested by centrifugation. Cell pellets were resuspended in 1/20th volume of buffer A (50 mM Tris-HCl (pH 8.0), 500 mM NaCl, 25 mM imidazole, 10% (vol/vol) glycerol) containing the Complete™ cocktail of protease inhibitors (Roche). Cells were lysed by six passages through a cell disruptor (Constant Systems Limited) at 20 kPsi, and cell debris were pelleted by centrifugation at 40,000g for 30 min at 4 °C. The centrifugation supernatant was loaded on a Ni-NTA agarose resin (Qiagen) equilibrated with buffer A. After extensive washing with buffer A, the fusion protein was eluted with a linear 0–100% gradient of buffer B (50 mM Tris-HCl (pH 8.0), 300 mM NaCl, 500 mM imidazole, 10% (vol/vol) glycerol) over 10 column volumes. Peak fractions were pooled, mixed with a 1:100 dilution of a His-tagged Ulp1 (SUMO) protease preparation (Uehara et al., 2010) and dialyzed overnight at 4 °C in buffer C (50 mM Tris-HCl (pH 8.0), 300 mM NaCl, 10% (vol/vol) glycerol). Cleavage reactions were passed through Ni-NTA resin to remove free His-SUMO tag and His-Ulp1, and untagged protein was collected in the flow through. Flow-through fractions were concentrated with Amicon Ultra Centrifugal filter units with a molecular weight cutoff of 10 kDa (Millipore) and were injected onto an ENrich™ SEC650 10x300 gel-filtration column (Biorad). Proteins were eluted with buffer D (25 mM Tris-HCl (pH 8.0), 150 mM NaCl) and again concentrated with Amicon Ultra Centrifugal filter units. Protein concentration was measured using absorbance at 280 nm.

4.3. Mass spectrometry analyses

Liquid Chromatography Electrospray Ionization Mass Spectrometry (LC/ESI-MS) was applied for quality control of intact proteins by using a 6210 LC/ESI-TOF mass spectrometer interfaced with an HPLC binary pump system (Agilent Technologies). Mass spectra were recorded in the 300–3200 *m/z* range, in the positive ion mode with spectra in the profile mode. The MS spectra were acquired and the data processed with MassHunter workstation software (v. B.02.00, Agilent

Technologies) and with GPMW software (v. 7.00b2, Lighthouse Data, Denmark).

Just before analysis the protein samples were diluted in acidic denaturing conditions to a final concentration of 5 µM with solution E (0.03% TFA in water). Samples were cooled to 10 °C in the autosampler and the analysis was run by injecting 4 µl of each sample. They were first trapped and desalted on a reverse phase-C8 cartridge (Zorbax 300SB-C8, 5µm, 300 µm ID × 5 mm, Agilent Technologies) for 3 min at a flow rate of 50 µl/min with 100% solvent E and then eluted with 70% solvent F (95% acetonitrile-5% water-0.03% TFA) at flow rate of 50 µl/min for MS detection.

4.4. SEC-MALLS analyses

SEC-MALLS runs were performed using a ENrich™ SEC650 10 × 300 gel-filtration column (Biorad) connected to an analytic system including a L2130 pump (Hitachi), a L-2400 UV detector (Hitachi), an Optilab T-rEX refractometer (Wyatt technologies) and a DAWN HELEOS-II multi angle light scattering detector (Wyatt technologies). Prior to injection, columns and systems were equilibrated in 5 to 10 column volumes of buffer D. Fifty-µl of protein samples concentrated at a minimum of 2 mg/ml were injected with a constant flow rate of 0.5 ml/min. Protein concentration was quantified online by measuring the differential refractive index and using an averaged refractive index increment *dn/dc* of 0.185 ml/g. Accurate weight-averaged molar masses (MW) determination was performed with the Astra 6 software (Wyatt Technologies) and curves were represented with Excel (Microsoft office 2013).

4.5. Protein crystallization and X-ray data collection

High-throughput crystallization trials were performed with a Cartesian PixSys 4200 crystallization robot (Genomic Solutions, U.K.). Hanging drops containing 100 nl of protein (40, 20 or 10 mg/ml) and 100 nl of reservoir solution were set up in 96-well Crystal Quick plates (Greiner) and incubated at 20 °C. Initial crystal hits were refined manually by setting up hanging drops containing 1 µl of protein (40 or 20 mg/ml) and 1 µl of reservoir solution in 24-well plates (Molecular Dimensions) incubated at 20 °C. Large needle-shaped crystals (dimensions of about 40 × 40 × 400 µm) were finally obtained for GerMN1 (first GerMN domain) in 200 mM Na acetate, 21% (w/vol) PEG 3350. GerMN1 crystals appeared within 2 days and reached their full size within 7 days. The full-length soluble construct of GerM (GerM₂₆₋₃₆₆) yielded short 3D needles in 100 mM Hepes pH 7.2, 2.6 M NH₄SO₄. GerM₂₆₋₃₆₆ crystals appeared within 4 days and reached their full size within 2 weeks. Before X-ray diffraction data collection, crystals were soaked for < 5 min in the appropriate reservoir solution containing 10% (vol/vol) glycerol and 10% (vol/vol) ethylene glycol, and flash-frozen in liquid nitrogen. X-ray diffraction data were collected at the European Synchrotron Radiation Facility (ESRF, Grenoble, France), on the ID23eh1 and ID29 beamlines for GerMN1 and GerM₂₆₋₃₆₆ crystals, respectively. Experimental setup of the beamline and data quality of the collected images were monitored with MxCuBE (Gabadinho et al., 2010). Statistics on data collection and refinement are summarized in Table 1.

4.6. Structure determination and refinement

Diffraction data were indexed and scaled using the XDS program suite (Kabsch, 2010). GerMN1 crystals belong to the orthorhombic space group P2₁2₁2₁, with unit cell dimensions of 38.36 × 53.60 × 64.84 Å and a single molecule per asymmetric unit. *Ab initio* phase determination for GerMN1 was achieved using the ARCIMBOLDO_LITE program (Sammuto et al., 2013), which combines the location of model fragments like small α-helices with PHASER (McCoy et al., 2007) and density modification with SHELXE (Thorn and Sheldrick, 2013). We

first unsuccessfully started the structure search by using two 10-residue long polyalanine α -helices (default size), using a machine of 4 cores. Based on secondary structure predictions performed by the JPRED4 server (<http://www.compbio.dundee.ac.uk/jpred/>), we then searched for two α -helices containing 13 or 12 residues, using machines of 4 cores or 8 cores, respectively. Both strategies yielded an electron density map from the correct positioning of the two α -helices. The high quality of this map allowed automated building of the GerMN1 model (from T76 until D208) using Phenix (Terwilliger et al., 2008).

GerM1 crystals belong to the orthorhombic space group $P2_12_12_1$, with unit cell dimensions of $90.36 \times 103.94 \times 162.49$ Å and four molecules per asymmetric unit. Phase determination was carried out by the molecular replacement method with PHASER, using as a search model for the two GerMN domains the structure of GerMN1. The molecular replacement solution model was rebuilt de novo using PHENIX to prevent bias from the model.

The structures of GerMN1 and GerM₂₆₋₃₆₆ were completed by cycles of manual building with COOT (Emsley and Cowtan, 2004) and addition of water molecules with ARP/wARP (Langer et al., 2008). Several cycles of manual building and refinement with REFMAC (Murshudov et al., 2011), as implemented in the CCP4 program suite, were performed until R_{work} and R_{free} converged (Brünger, 1992). Stereochemical verification was performed with PROCHECK (Laskowski et al., 1993). The secondary structure assignment was verified with DSSP (Kabsch and Sander, 1983). Figures were generated with PyMol (<http://www.pymol.org>). Coordinates of the final refined models were deposited at the Protein Data Bank (PDB, <http://www.rcsb.org>) and were assigned PDB entry codes 6GZ8 and 6GZB for GerMN1 and GerM₂₆₋₃₆₆, respectively.

4.7. SAXS analyses

SAXS experiments were carried out at the BM29 beamline (ESRF, Grenoble, France) using a robotic sample changer and a Pilatus 1 M detector (Dectris, Baden-Daettwil, Switzerland) with a detector distance of 2.867 m. The scattering intensity, $I(s)$, was recorded in the range of the momentum transfer $0.03 < s < 4.92 \text{ nm}^{-1}$, where $s = (4\pi\sin\theta)/\lambda$, 2θ is the scattering angle and $\lambda = 1.0$ Å the X-ray wavelength (Pernot et al., 2013). The measurements were performed with the sample in buffer D at 20 °C using continuous flow operation over a total exposure time of 0.5 s divided into 10 individual frames to monitor for potential radiation damage. GerMN1 samples at five protein concentrations ranging from 10.4 to 0.63 mg/ml were measured to account for interparticle interactions. Since all samples measured for the different GerMN1 concentrations showed similar SAXS data for the s angles and no repulsive interparticle interference, the SAXS data at low angles from the 1.25 g/L sample were merged with $s > 1.44 \text{ nm}^{-1}$ intensities of the 10.4 g/L sample of GerMN1 using PRIMUS to produce the final GerMN1 experimental scattering profile.

The data were processed with ATSAS package (<https://www.embl-hamburg.de/biosaxs>) (Franke et al., 2017) using standard procedures, corrected for buffer contribution, and extrapolated to infinite dilution using the program PRIMUS. The forward scattering $I(0)$ and the radii of gyration R_g were evaluated using the Guinier approximation assuming that at very small angles ($sR_g < 1.3$) the intensity is represented as $I(s) = I(0) \exp(-sR_g^2/3)$. Both parameters were combined with protein concentration relative to bovine serum albumin standard to assess the GerMN molecular mass $MM_{I(0)}$. The entire scattering pattern was also computed using the indirect transform package GNOM that provides the maximum dimension of the particle D_{max} and the distance distribution function $p(r)$. The excluded volume of the hydrated particle (the Porod volume, V_p) was computed using the Porod invariant (Petoukhov et al., 2012). The GerMN molecular weight in solution was also calculated from the concentration-independent excluded Porod volume (MM_{porod}) assuming the 1.7 empirical ratio between V_p and the MM of a protein. The program CRY SOL was used to compute the

scattering from the GerMN1 crystal structure. The *ab initio* modeling program DAMMIF was employed for low-resolution shape generation, and 20 models were calculated in the slow mode, using standard settings. The program DAMAVER was used to superimpose individual structures, and to determine the averaged and the most probable reconstruction. The *ab initio* model was superimposed with the high-resolution crystal structure of GerMN1 using SUPCOMB.

Acknowledgments

We thank members of the Vernet laboratory for support, advice and encouragement. We thank Luca Signor for mass spectrometry analysis, Christoph Mueller (ESRF, beamline ID23eh1) and Nicolas Foos (ESRF, beamline ID29) for support in data collection. This work was supported by start-up funds provided by University of Technology Sydney to Christopher Rodrigues, and by funds provided by the French National Research Agency in the framework of the “Investissements d’avenir” program (ANR-15-IDEX-02) to Cecile Morlot. We acknowledge the platforms of the Grenoble Instruct center (ISBG; UMS 3518 CNRS-CEA-UGA-EMBL) supported by the French Infrastructure for Integrated Structural Biology Initiative FRISBI (ANR-10-INSB-05-02) and by the Grenoble Alliance for Integrated Structural Cell Biology GRAL (ANR-10-LABX-49-01) within the Grenoble Partnership for Structural Biology (PSB).

Author contributions

J.T., A.M., F.L., D.Z.R., C.D.A.R. and C.Mo. designed the research; J.T., A.M., F.L., C.C-M., B.L., C.M., C.D.A.R. and C.Mo performed the research; J.T., A.M., F.L., C.C-M., C.M., C.D.A.R. and C.Mo. analyzed the data; C.D.A.R. and C.Mo. wrote the paper; J.T., A.M., F.L., C.C-M., B.L., C.M., and D.Z.R. helped revise the paper.

Conflict of interest

The authors declare no conflict of interest.

Appendix A. Supplementary data

Supplementary data to this article can be found online at <https://doi.org/10.1016/j.jsb.2018.09.010>.

References

- Bergeron, J.R.C., Worrall, L.J., De, S., Sgourakis, N.G., Cheung, A.H., Lameignere, E., Okon, M., Wasney, G.A., Baker, D., McIntosh, L.P., Strynadka, N.C.J., 2015. The modular structure of the inner-membrane ring component PrgK facilitates assembly of the Type III secretion system basal body. *Structure* 23, 161–172.
- Brünger, A.T., 1992. Free R value: a novel statistical quantity for assessing the accuracy of crystal structures. *Nature* 355, 472–475.
- Camp, A.H., Losick, R., 2008. A novel pathway of intercellular signalling in *Bacillus subtilis* involves a protein with similarity to a component of type III secretion channels. *Mol. Microbiol.* 69, 402–417.
- Camp, A.H., Losick, R., 2009. A feeding tube model for activation of a cell-specific transcription factor during sporulation in *Bacillus subtilis*. *Genes Dev.* 23, 1014–1024.
- Chandran, V., 2013. Type IV secretion machinery: molecular architecture and function. *Biochem. Soc. Trans.* 41, 17–28.
- Costa, T.R.D., Felisberto-Rodrigues, C., Meir, A., Prevost, M.S., Redzej, A., Trokter, M., Waksman, G., 2015. Secretion systems in Gram-negative bacteria: structural and mechanistic insights. *Nat. Rev. Microbiol.* 13, 343–359.
- Doan, T., Morlot, C., Meisner, J., Serrano, M., Henriques, A.O., Moran, J.C.P., Rudner, D.Z., 2009. Novel secretion apparatus maintains spore integrity and developmental gene expression in *Bacillus subtilis*. *PLoS Genet.* 5, e1000566.
- Emsley, P., Cowtan, K., 2004. Coot: model-building tools for molecular graphics. *Acta Crystallogr. D Biol. Crystallogr.* 60, 2126–2132.
- Franke, D., Petoukhov, M.V., Konarev, P.V., Panjkovich, A., Tuukkanen, A., Mertens, H.D.T., Kikhney, A.G., Hajizadeh, N.R., Franklin, J.M., Jeffries, C.M., Svergun, D.I., 2017. ATSAS 2.8: a comprehensive data analysis suite for small-angle scattering from macromolecular solutions. *J. Appl. Crystallogr.* 50, 1212–1225.
- Gabadinho, J., Beteva, A., Guijarro, M., Rey-Bakaikoa, V., Spruce, D., Bowler, M.W., Brockhauser, S., Flot, D., Gordon, E.J., Hall, D.R., Lavault, B., McCarthy, A.A., McCarthy, J., Mitchell, E., Monaco, S., Mueller-Dieckmann, C., Nurizzo, D., Ravelli,

- R.B.G., Thibault, X., Walsh, M.A., Leonard, G.A., McSweeney, S.M., 2010. MxCuBE: a synchrotron beamline control environment customized for macromolecular crystallography experiments. *J. Synchrotron Radiat.* 17, 700–707.
- Guillot, C., Moran, C.P., 2007. Essential Internal Promoter in the spoIIIA Locus of *Bacillus subtilis*. *J. Bacteriol.* 189, 7181–7189.
- Higgins, D., Dworkin, J., 2012. Recent progress in *Bacillus subtilis* sporulation. *FEMS Microbiol. Rev.* 36, 131–148.
- Hilbert, D.W., Piggot, P.J., 2004. Compartmentalization of gene expression during *Bacillus subtilis* spore formation. *Microbiol. Mol. Biol. Rev.* 68, 234–262.
- Holm, L., Rosenström, P., 2010. Dali server: conservation mapping in 3D. *Nucleic Acids Res.* 38, W545–W549.
- Kabsch, W., 2010. XDS. *Acta Crystallogr. D Biol. Crystallogr.* 66, 125–132.
- Kabsch, W., Sander, C., 1983. Dictionary of protein secondary structure: pattern recognition of hydrogen-bonded and geometrical features. *Biopolymers* 22, 2577–2637.
- Langer, G.G., Cohen, S.X., Lamzin, V.S., Perrakis, A., 2008. Automated macromolecular model building for X-ray crystallography using ARP/wARP version 7. *Nat. Protoc.* 3, 1171–1179.
- Laskowski, R.A., MacArthur, M.W., Moss, D.S., Thornton, J.M., 1993. PROCHECK: a program to check the stereochemical quality of protein structures. *J. Appl. Crystallogr.* 26, 283–291.
- Levdikov, V.M., Blagova, E.V., McFeat, A., Fogg, M.J., Wilson, K.S., Wilkinson, A.J., 2012. Structure of components of an intercellular channel complex in sporulating *Bacillus subtilis*. *Proc. Natl. Acad. Sci.* 109, 5441–5445.
- Londoño-Vallejo, J.-A., Fréhel, C., Stragier, P., 1997. spoIIQ, a forespore-expressed gene required for engulfment in *Bacillus subtilis*. *Mol. Microbiol.* 24, 29–39.
- Marblestone, J.G., Edavettal, S.C., Lim, Y., Lim, P., Zuo, X., Butt, T.R., 2006. Comparison of SUMO fusion technology with traditional gene fusion systems: enhanced expression and solubility with SUMO. *Protein Sci. Publ. Protein Soc.* 15, 182–189.
- McCoy, A.J., Grosse-Kunstleve, R.W., Adams, P.D., Winn, M.D., Storoni, L.C., Read, R.J., 2007. Phaser crystallographic software. *J. Appl. Crystallogr.* 40, 658–674.
- Meisner, J., Wang, X., Serrano, M., Henriques, A.O., Moran, C.P., 2008. A channel connecting the mother cell and forespore during bacterial endospore formation. *Proc. Natl. Acad. Sci.* 105, 15100–15105.
- Meisner, J., Maehigashi, T., André, I., Dunham, C.M., Moran, C.P., 2012. Structure of the basal components of a bacterial transporter. *Proc. Natl. Acad. Sci.* 109, 5446–5451.
- Morlot, C., Rodrigues, C.D.A., 2018. The new kid on the block: a specialized secretion system during bacterial sporulation. *Trends Microbiol.* 26, 663–676.
- Murshudov, G.N., Skubák, P., Lebedev, A.A., Pannu, N.S., Steiner, R.A., Nicholls, R.A., Winn, M.D., Long, F., Vagin, A.A., 2011. REFMAC5 for the refinement of macromolecular crystal structures. *Acta Crystallogr. D Biol. Crystallogr.* 67, 355–367.
- Pernot, P., Round, A., Barrett, R., De Maria Antolinos, A., Gobbo, A., Gordon, E., Huet, J., Kieffer, J., Lentini, M., Mattenet, M., Morawe, C., Mueller-Dieckmann, C., Ohlsson, S., Schmid, W., Surr, J., Theveneau, P., Zerrad, L., McSweeney, S., 2013. Upgraded ESRF BM29 beamline for SAXS on macromolecules in solution. *J. Synchrotron Radiat.* 20, 660–664.
- Petoukhov, M.V., Franke, D., Shkumatov, A.V., Tria, G., Kikhney, A.G., Gajda, M., Gorba, C., Mertens, H.D.T., Konarev, P.V., Svergun, D.I., 2012. New developments in the ATSAS program package for small-angle scattering data analysis. *J. Appl. Crystallogr.* 45, 342–350.
- Portaliou, A.G., Tsolis, K.C., Loos, M.S., Zorzini, V., Economou, A., 2016. Type III secretion: building and operating a remarkable nanomachine. *Trends Biochem. Sci.* 41, 175–189.
- Rigden, D.J., Galperin, M.Y., 2008. Sequence analysis of GerM and SpoVS, uncharacterized bacterial “sporulation” proteins with widespread phylogenetic distribution. *Bioinforma. Oxf. Engl.* 24, 1793–1797.
- Rodrigues, C.D.A., Ramírez-Guadiana, F.H., Meeske, A.J., Wang, X., Rudner, D.Z., 2016b. GerM is required to assemble the basal platform of the SpoIIIA–SpoIIQ transenvelope complex during sporulation in *Bacillus subtilis*. *Mol. Microbiol.* 102, 260–273.
- Rodrigues, C.D.A., Henry, X., Neumann, E., Kurauskas, V., Bellard, L., Fichou, Y., Schanda, P., Schoehn, G., Rudner, D.Z., Morlot, C., 2016a. A ring-shaped conduit connects the mother cell and forespore during sporulation in *Bacillus subtilis*. *Proc. Natl. Acad. Sci.* 113, 11585–11590.
- Sammito, M., Millán, C., Rodríguez, D.D., de Ilarduya, I.M., Meindl, K., De Marino, I., Petrillo, G., Buey, R.M., de Pereda, J.M., Zeth, K., Sheldrick, G.M., Uson, I., 2013. Exploiting tertiary structure through local folds for crystallographic phasing. *Nat. Methods* 10, 1099–1101.
- Sammons, R.L., Slynn, G.M., Smith, D.A., 1987. Genetical and molecular studies on gerM, a new developmental locus of *Bacillus subtilis*. *J. Gen. Microbiol.* 133, 3299–3312.
- Schraidt, O., Marlovits, T.C., 2011. Three-Dimensional model of Salmonella’s needle complex at subnanometer resolution. *Science* 331, 1192–1195.
- Slynn, G.M., Sammons, R.L., Smith, D.A., Moir, A., Corfe, B.M., 1994. Molecular genetical and phenotypical analysis of the gerM spore germination gene of *Bacillus subtilis* 168. *FEMS Microbiol. Lett.* 121, 315–320.
- Tan, I.S., Ramamurthi, K.S., 2014. Spore formation in *Bacillus subtilis*. *Environ. Microbiol. Rep.* 6, 212–225.
- Terwilliger, T.C., Grosse-Kunstleve, R.W., Afonine, P.V., Moriarty, N.W., Zwart, P.H., Hung, L.-W., Read, R.J., Adams, P.D., 2008. Iterative model building, structure refinement and density modification with the PHENIX AutoBuild wizard. *Acta Crystallogr. D Biol. Crystallogr.* 64, 61–69.
- Thorn, A., Sheldrick, G.M., 2013. Extending molecular-replacement solutions with SHELXE. *Acta Crystallogr. D Biol. Crystallogr.* 69, 2251–2256.
- Uehara, T., Parzych, K.R., Dinh, T., Bernhardt, T.G., 2010. Daughter cell separation is controlled by cytotkinetic ring-activated cell wall hydrolysis. *EMBO J.* 29, 1412–1422.
- Worrall, L.J., Hong, C., Vuckovic, M., Deng, W., Bergeron, J.R.C., Majewski, D.D., Huang, R.K., Spreter, T., Finlay, B.B., Yu, Z., Strynadka, N.C.J., 2016. Near-atomic-resolution cryo-EM analysis of the Salmonella T3S injectisome basal body. *Nature* 540, 597–601.
- Yokoyama, K., Muneyuki, E., Amano, T., Mizutani, S., Yoshida, M., Ishida, M., Ohkuma, S., 1998. V-ATPase of *Thermus thermophilus* Is Inactivated during ATP Hydrolysis but Can Synthesize ATP. *J. Biol. Chem.* 273, 20504–20510.
- Youngman, P.J., Perkins, J.B., Losick, R., 1983. Genetic transposition and insertional mutagenesis in *Bacillus subtilis* with *Streptococcus faecalis* transposon Tn917. *Proc. Natl. Acad. Sci.* 80, 2305–2309.
- Zeytuni, N., Hong, C., Flanagan, K.A., Worrall, L.J., Theiltges, K.A., Vuckovic, M., Huang, R.K., Massoni, S.C., Camp, A.H., Yu, Z., Strynadka, N.C.J., 2017. Near-atomic resolution cryoelectron microscopy structure of the 30-fold homooligomeric SpoIIAG channel essential to spore formation in *Bacillus subtilis*. *Proc. Natl. Acad. Sci. U. S. A.* 114, E7073–E7081.
- Zeytuni, N., Flanagan, K.A., Worrall, L.J., Massoni, S.C., Camp, A.H., Strynadka, N.C.J., 2018b. Structural and biochemical characterization of SpoIIAF, a component of a sporulation-essential channel in *Bacillus subtilis*. *J. Struct. Biol.* 204, 1–8.
- Zeytuni, N., Flanagan, K.A., Worrall, L.J., Massoni, S.C., Camp, A.H., Strynadka, N.C.J., 2018a. Structural characterization of SpoIIAB sporulation-essential protein in *Bacillus subtilis*. *J. Struct. Biol.* 202, 105–112.